Series Dual-Fed Continuous Transverse Stub Array Enabled by a Reflective Luneburg Lens with Enhanced Multi-Beam Operation

Christos Bilitos, Xavier Morvan, Ronan Sauleau, Enrica Martini, Stefano Maci, D. Gonzalez-Ovejero

Series Dual-Fed Continuous Transverse Stub Array Enabled by a Reflective Luneburg Lens with Enhanced Multi-Beam Operation

Christos Bilitos, *Student, IEEE,* Xavier Morvan, Ronan Sauleau, *Fellow, IEEE,* Enrica Martini, *Senior Member, IEEE,* Stefano Maci, *Fellow, IEEE,* and David González-Ovejero, *Senior Member, IEEE*

***Abstract*—This paper introduces an all-metal series dual-fed continuous transverse stub (CTS) array that enables multi-beam operation at K-band. This capability is obtained by utilizing a reflecting Luneburg lens (RLL) beamformer made of two stacked circular parallel plate waveguides (PPWs). The bottom PPW hosts a graded index medium that collimates the rays coupled by a corner reflector to the top PPW, where the CTS array is located. This design capitalizes on the RLL's rotational symmetry, employing a circular array of feeds to generate multiple planar wavefronts that illuminate the CTS array across a 360° range. Consequently, a new series-fed CTS array has been introduced to ensure high aperture efficiency when excited from diametrically opposed ends. The appropriate selection of the feeds, combined with the rotation of the CTS plane, enables the generation of simultaneous independent beams with continuous scanning. This architecture enhances the capabilities of conventional variable inclination CTS arrays. A prototype has been fabricated and tested, demonstrating excellent performance between 17.3 and 21.2 GHz, with an aperture efficiency of 43.5-58% and a radiation efficiency of 90%. The antenna achieves scanning up to 55° in azimuth and from 5° to 65° in elevation through port switching, and full-azimuthal coverage with the added mechanical rotation. This design is particularly significant for K-band low-earth orbit (LEO) high-throughput satellite communications.**

***Index Terms*—beam-scanning, broadband antenna, continuous transverse stub array, K-band, metalens, multi-beam antenna, reflecting Luneburg lens, satellite communications.**

I. Introduction

THE growing demand for seamless connectivity and higher data rates has driven a shift towards heterogeneous space and terrestrial networks and the utilization of higher frequency bands, such as the K-band [1]. In this context, low-earth orbit (LEO) high-throughput satellite communications (SATCOMs) [2] require novel antenna concepts to maintain the connectivity both in the space and ground segments. Multi-beam architectures with wide coverage are particularly crucial as they can reduce the number of antennas onboard the satellite [3]. Additionally, due to its integration in moving platforms, the antenna system in the ground segment needs to be low-profile and strike an optimal trade-off between fabrication complexity, power consumption, material losses, and bandwidth.

Continuous transverse stub (CTS) arrays [4] were proposed in the 1990s by Milroy to meet the requirements above [5]–[7] and have been widely utilized in SATCOM. Depending on the array feeding scheme, CTS arrays can be categorized as parallel-fed [8]–[14] or series-fed [15]–[17]. Parallel-fed CTS arrays operate over larger bandwidths with a fixed pointing angle, while series-fed CTS arrays offer a lower-profile solution with wide-angle frequency scanning [18]. Series-fed CTS arrays typically consist of a double-layer structure, comprising two stacked parallel plate waveguides (PPWs) or substrate integrated waveguides. The bottom layer includes a beamformer that generates a planar wavefront in the top layer, which hosts the slot array. Continuous scanning along a given contour can be achieved by introducing an inclination between the propagating wavefront exciting the CTS and the long slots, as in variable inclination CTS (VICTS) arrays [19]. To that end, most solutions feature a mechanical rotation between the two PPWs [15], [20].

The planar wavefront utilized to feed the slots in VICTS arrays is commonly generated in one direction by using a corporate feed network (CFN) in the bottom PPW [15], [20]. However, planar wavefronts with different directions may also be generated by using quasi-optical (QO) beamformers in PPWs, such as pillbox systems [8]–[14], [21], [22] and flat Luneburg lenses (LLs) [23]–[29]. Both solutions, when appropriately combined with a radiating aperture like the CTS, can generate pencil beams. LLs can create planar wavefronts with different azimuthal directions without suffering from scan loss. However, to achieve pencil beams, the radiating aperture needs to be placed after the lens, resulting in an increased antenna footprint [26], [29] and low aperture efficiency. Pillbox systems, on the other hand, have a more compact architecture, with the beamformer and antenna sharing a common aperture. These systems consist of two stacked PPWs connected by a 180^o PPW bend with a parabolic profile, transforming a cylindrical wavefront generated by a primary feed in the bottom PPW into a plane wave in the top one. However, coma phase errors increase the side-lobe level (SLLs) when scanning

Manuscript received May 17 2024. This work has been supported in part by the Agence de l'Innovation de Défense (AID), the European Union through the European Regional Development Fund (ERDF), CNRS, the French region of Brittany, Ministry of Higher Education and Research, Conseils Départementaux d'Ille-et-Vilaine and Côtes d'Armor, Rennes Métropole, and Lannion Trégor Communauté, through the CPER Projects SOPHIE / STIC & Ondes, CyMoCod. This work has also received support from the French National Research Agency (ANR) through the project AROMA with reference ANR-22-CE24-0013.

C. Bilitos, X. Morvan, R. Sauleau, and D. González-Ovejero are with Univ Rennes, CNRS, Institut d'Électronique et des Technologies du numéRique (IETR) - UMR 6164, F-35000 Rennes, France. (e-mail: david.gonzalez-ovejero@univ-rennes.fr).

E. Martini and S. Maci are with Department of Information Engineering and Mathematics, University of Siena, Italy (e-mail: macis@dii.unisi.it).

the beam by moving the feed position in the focal plane.

To address the aforementioned challenges, the reflecting Luneburg lens (RLL) was introduced in [30]. The RLL comprises two vertically stacked circular PPWs. The lower PPW is filled with a graded index (GRIN) medium, which exhibits cylindrical symmetry and enables full azimuthal scanning. The GRIN medium guides the rays along curvilinear trajectories so that, upon encountering a reflecting boundary, they emerge parallel in the upper PPW as a plane wave. Different approaches for realizing the RLL medium have already been documented in the literature, such as geodesics [31] and metallic bed-of-nails (BoN) [32].

This work leverages the azimuthal scanning capabilities of the RLL to efficiently excite a specially modified series dual-fed CTS array. By switching between multiple ports placed in the lower PPW, the proposed antenna can radiate multiple pencil beams. Each port excites one of the ridge waveguide feeds arrayed along a focal ring to generate planar wavefronts with different directions in the upper PPW. The angles of these wavefronts relative to the orientation of the slot array determine the direction of the beam for each port. Therefore, port-switching allows beam scanning without the need for mechanical rotation between the layers, although rotation can still be used to increase coverage. Furthermore, for the first time in the literature, the CTS array has been adapted to benefit from bi-directional excitation, taking advantage of the RLL's 360° azimuthal scanning capabilities, all while optimizing the aperture efficiency in this scenario. Such features may be of interest to systems that handle handover processes.

The paper is structured as follows. Section II presents the antenna structure comprised by the RLL, the feeding system and the CTS array. Section III discusses the numerical simulation results of the antenna and compares it with experimental measurements for the input reflection coefficients and coupling matrix, radiation patterns and scanning performance. Finally, the conclusions are drawn in Section IV.

II. Antenna Design

The proposed antenna, depicted in Fig. 1(a), operates over a frequency range from 17.3 GHz to 21.2 GHz catering for both civil and military downlink needs in SATCOM. The circular structure has a diameter of $D = 200$ mm and a height of $H = 22.7$ mm. It can be divided into three structural blocks, labelled as P1, P2 and P3 in the exploded view of Fig. 1(a). Blocks P1 and P2 conform the bottom PPW, which accommodates the RLL beamformer, while blocks P2 and P3 constitute the CST array. The three blocks are entirely metallic, which eliminates dielectric losses and ensures mechanical robustness.

Before delving into the details of the design, let us succinctly explain the working mechanism of the antenna. The RLL beamformer in the bottom PPW exploits a BoN structure to realize the RLL GRIN medium, as explained in Section II-A. The cylindrically symmetric GRIN medium guides the rays launched by a primary source, placed in a focal ring, until the circular conductive rim such that they emerge collimated in the upper PPW. The coupling between the RLL and the top PPW is achieved effectively by a corner reflector,

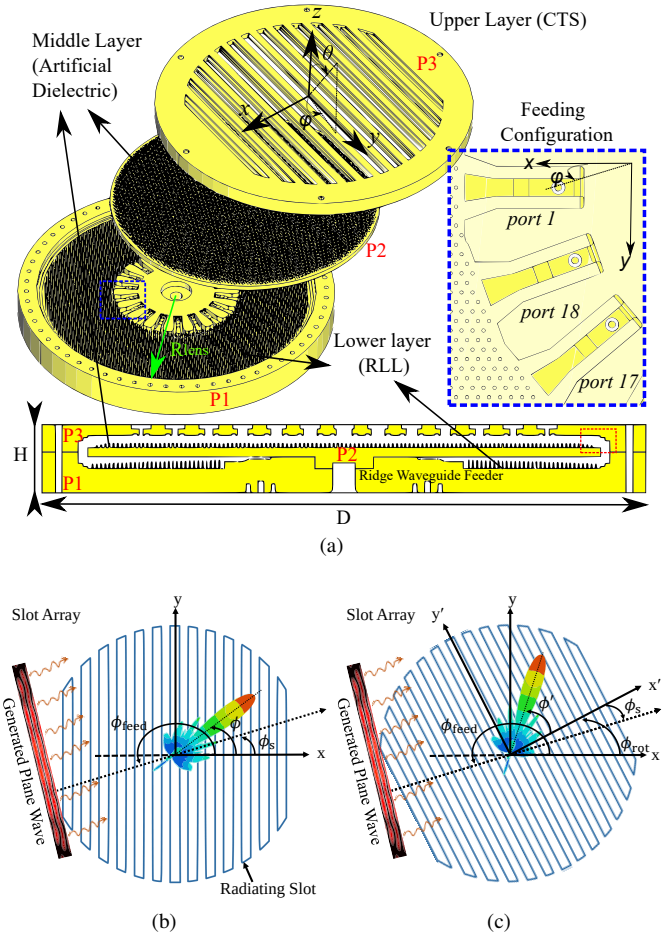

Fig. 1. (a) Perspective and side views of the proposed antenna architecture. Operating principle of the series-fed CTS array under variable inclination ϕ_s of the impinging slow-wave wavefront with respect to the stub array (b) without and (c) with rotation of the block P3 with the long slots (top views).

as shown in the side view of Fig. 1(a) and the zoom in Fig. 2(d). The planar wavefront generated in the upper PPW is then gradually radiated by the long slot array as a pencil beam, the direction of which will be determined by the angle ϕ_s between the plane wave and the array of slots, as depicted in Fig. 1(b).

In VICTS arrays, this relative angle is obtained by introducing mechanical rotation between the beamforming network and the stub array [15], enabling continuous scanning. However, in our design, the angle between the propagating plane wave and the slots can be simply controlled by introducing multiple feeds in the RLL inner focal ring (right inset in Fig. 1(a)). Assuming ϕ_{feed} the angle of the feed with respect to the x-axis, each feed generates a planar wavefront in a different direction defined by the relative angle $\phi_s = \pi + \phi_{\text{feed}}$ as presented in Fig. 1(b). To achieve this, the structure in Fig. 1(a) incorporates 18 feeds equispaced at an angle of 20°, as detailed in Section II-B. Out of these feeds, up to 5 pairs of diametrically opposed ports can be excited at a time to radiate a beam for a fixed orientation of the CTS. A sequential excitation of these ports yields beam scanning via port switching, while simultaneous excitation results in a multi-beam operation. Furthermore, the scanning range can be significantly enhanced by mechanically rotating the upper

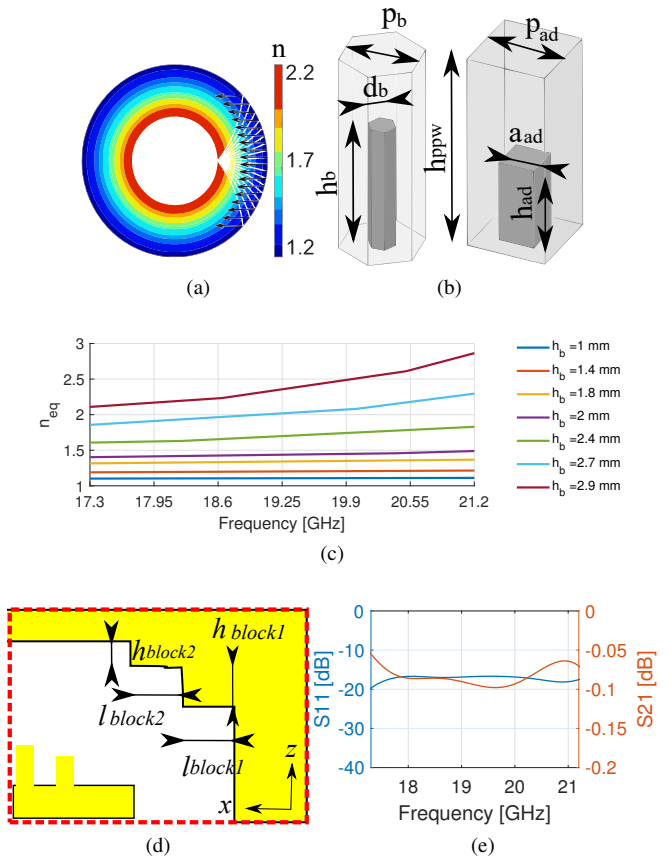

Fig. 2. (a) Ray-paths in the bottom PPW (white lines), in the top PPW (black arrows), and color map showing the refractive index values for the RLL's GRIN medium for a source placed at its inner focal ring. (b) Hexagonal unit-cell with dimensions $p_b = 1.4\,\text{mm}$, $d_b = 0.43\,\text{mm}$ and $h_{ppw} = 4\,\text{mm}$, (left); unit-cell for the artificial dielectric with dimensions $p_{ad} = 1.4\,\text{mm}$, $a_{ad} = 0.63\,\text{mm}$ and $h_{ppw} = 4\,\text{mm}$ (right). (c) Equivalent refractive index of the hexagonal unit-cell as a function of frequency for different values of h_b. (d) Side view of the corner reflector with dimensions $l_{block1} = 1.6\,\text{mm}$, $h_{block1} = 1.8\,\text{mm}$, $l_{block2} = 1.6\,\text{mm}$ and $h_{block2} = 0.7\,\text{mm}$. (e) Magnitude of the input reflection (solid blue line) and transmission (solid red line) coefficients in dB for the corner reflector transition between the two layers.

layer an angle ϕ_{rot} with respect to the x-axis, which results in $\phi_{\text{s}} = \pi + \phi_{\text{feed}} - \phi_{\text{rot}}$. This surpasses the contour restrictions of conventional VICTS arrays.

Finally, the series dual-fed CTS is described in Section II-C. While the RLL is responsible for collimation in the H-plane, the long slots produce the narrow beam in the E-plane. Additionally, the series configuration enables frequency scanning for all the beams, further expanding the field of view.

A. Reflecting Luneburg Lens

The RLL beamformer and corner reflector in this antenna system reside within the lower PPW (comprised of blocks P1 and P2 in Fig. 1(a)). The refractive index profile of the RLL was analytically derived in [30] and reads as

$$n(r) = n_{up}\left(\frac{-1+\sqrt{1+8(r/R_{\text{lens}})^2}}{2\left((r/R_{\text{lens}})^2\right)}\right)^{3/2}, \qquad (1)$$

where n_{up} is the equivalent refractive index of the upper PPW, r is the radial distance and R_{lens} is the radius of the lens. Since the refractive index value at the rim of the lens matches that of the top PPW, we can easily couple the power to it using a corner reflector. The azimuthally symmetric GRIN medium described by (1) guides the rays emitted from a source at the focal circumference (rim of the lens) along curvilinear paths. These rays then impinge on a circular reflecting boundary at an angle of arrival, causing them to emerge parallel to each other in the top PPW. This mechanism is shown in Fig. 1(b) of [30]. Although the exact focus is at the periphery of the lens, the RLL also presents an inner focal ring at a radial distance $r = 0.46\,R$. The operation of the lens does not change significantly when the source is placed in this ring; that is, a planar wavefront is still generated in the upper PPW, as depicted in Fig. 2(a). Therefore, one can omit the center-most part of the structure and place the sources inside the lens, reducing the maximum required refractive index to $n(0.46R) = 1.86\,n_{up}$. More importantly, in this configuration, diametrically opposed sources do not block each other while coupling power to the upper PPW. This constitutes a key advantage compared to classical Luneburg lenses.

A BoN with hexagonal lattice [33]–[35] is used here to realize the GRIN medium of the RLL. As shown in the left side of Fig. 2(b), the periodic inclusions are placed in the bottom PPW with a height of $h_{ppw} = 4\,\text{mm}$ and consist of hexagonal metallic posts placed at the centers of the hexagonal unit cells. This type of lattice has more symmetry axes (six instead of the four present in a Cartesian lattice) [34]. The greater number of symmetry axes provides a more isotropic behavior for the unit-cell, which becomes particularly significant at frequencies where the unit-cells are not very small relative to the wavelength. A hexagonal lattice also enables an increase in the density of the unit-cells, thus increasing the resolution of the GRIN medium. Furthermore, the realization complexity is not significantly affected compared to the more conventional BoN with a rectangular lattice.

The unit-cell was simulated using an eigenmode solver [36], where we set the appropriate boundary conditions on the hexagonal walls of the unit-cell. From the dispersion diagram one can extract the equivalent refractive index, which is depicted in Fig. 2(c) as a function of frequency for different post heights h_b over the frequency range of interest. One can observe that $h_b = 2.85\,\text{mm}$ is sufficient to achieve the highest refractive index value $n(0.46R) = 2.2$ at the central frequency of $19.25\,\text{GHz}$ for a source positioned at the inner focal ring when $n_{up} = 1.2$. The rationale behind this value of n_{up} for the top PPW will be provided in the next section. Additionally, Fig. 2(c) illustrates the effects of dispersion, which are more pronounced for taller posts and could limit the bandwidth of operation of the lens. These effect may be mitigated by using a unit-cell with higher symmetries, as in [32]. However, considering the lens radius of $R_{\text{lens}} = 5.5\lambda_0$, where λ_0 is the free space wavelength at the center frequency, and the requested relative bandwidth of 20%, the hexagonal unit-cell with conventional symmetry provides a good trade-off between performance and fabrication complexity (simpler here than in the higher symmetric case).

The upper PPW should support a slow wave to excite the series-fed CTS array [37]. The required equivalent refractive index of $n_{up} = 1.2$ has been obtained using the BoN depicted

TABLE I
DIMENSION OF THE COAXIAL TO RIDGE WAVEGUIDE TRANSITION

Variable	l_1	l_2	l_3	l_4	l_5	w_1	w_2
Value (mm)	3.29	3.71	2	2.18	3.99	5.4	8.3
Variable	h_1	h_2	h_3	d_1	d_2	r_1	r_2
Value (mm)	3.14	3.34	2.4	0.9	1.8	2.2	3.49

in the right side of Fig. 2(b). This BoN consists of metallic square posts with a width of $a_{ad} = 0.63$ mm and a height of $h_{ad} = 1.46$ mm, arranged in a Cartesian lattice with periodicity $p_{ad} = 1.4$ mm. The power between the two PPW layers is coupled using a corner reflector. An important factor impacting its design is the thickness of the middle metallic plate (P2 in Fig. 1(a)), which must be sufficient to ensure structural rigidity and allow for the milling of the square posts on the top side without deformations. This thickness adds an extra optical path to the theoretical ray paths presented in [30]. To compensate for this effect, the dimensions of the corner reflector sections, presented in Fig. 2(d) are optimized ($l_{block1} = 1.6$ mm, $h_{block1} = 1.8$ mm, $l_{block2} = 1.6$ mm and $h_{block2} = 0.7$ mm) to minimize the phase errors associated with the additional optical path. The magnitudes of the reflection and transmission coefficients of the corner reflector are depicted in Fig. 2(e) with blue and red lines, respectively, over the frequency range of interest. This lens beamformer is excited by a circular array of feeds positioned at the inner focal ring, as described in the next section.

B. Feeding System

The array of feeds at the RLL's inner focal ring is depicted in Fig. 1(a) (block P1). The chosen solution relies on ridge waveguides, which are preferred over typical rectangular waveguides due to their greater compactness. This enables the potential accommodation of a larger number of feeds and enhances the angular resolution in azimuth. Specifically, to adhere to the cutoff frequency of the conventional rectangular waveguide at the lower frequency (17.3 GHz), the resulting waveguides would need to be at least 8.7 mm wide. This minimum width would allow for a maximum of 14 feeds, thereby impacting the level of overlap between adjacent beams and limiting the angular resolution in the azimuth plane to 25.7°. Hence, a ridge waveguide is selected as the feeding mechanism for the lens.

The ridge waveguides are vertically excited by a coaxial connector from the bottom side of part P1. Fig. 3(a) depicts the focal ring array, featuring a total of 18 feeders spaced at angular increments of 20° for ϕ_{feed}, which represents the angle of the feed with respect to the x-axis (Fig. 1(b)). The ports are numbered following a clockwise scheme. The top and side views of the coaxial-to-ridge transition are shown in the insets of Fig. 3(b). The dimensions of the matching section, presented in Table I, are optimized to match the impedance of the coaxial connector to that of the RLL in the inner focal region. Fig. 3(b) shows the magnitude of the input reflection coefficient for the coaxial-to-ridge transition when located in the inner focal region of the lens.

To showcase the illumination of the lens, we analyze a simplified structure, consisting of a half-lens with the top

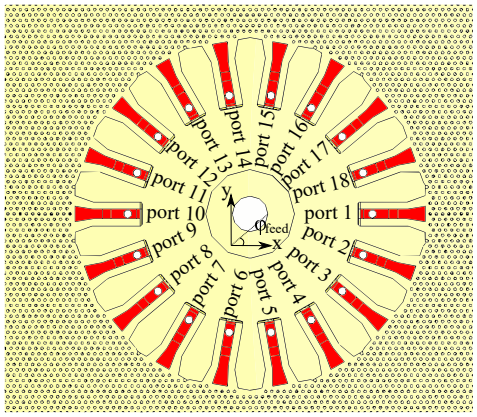

(a)

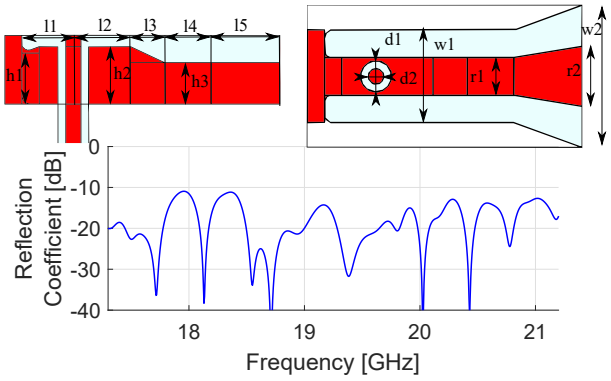

(b)

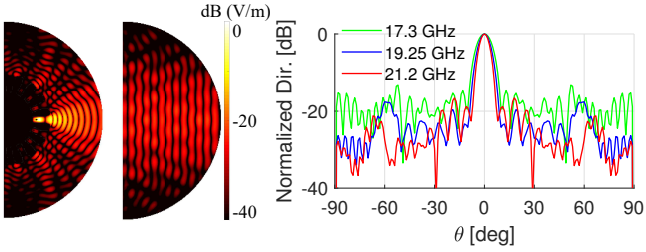

(c) (d)

Fig. 3. (a) Port configuration for the lens feeding system. The ports are placed at 20° increments of the angle ϕ, totaling 18 ports numbered clockwise. (b) Magnitude of the input reflection coefficient in dB for the coaxial-to-ridge transition when located in the inner focal region of the lens. The top-left and top-right insets show the side and top views, respectively, of the coaxial-to-ridge transition. The dimensions of the matching section are presented in Table I. (c) Real part of the vertical component of the electric field $Re(E_z)$ in logarithmic scale for (left) the bottom PPW and (right) the top PPW at $f = 19.25$ GHz. (d) Normalized directivity on the H-plane cut at $f = 19.25$ GHz (blue), $f = 17.3$ GHz (green) and at $f = 21.2$ GHz (red).

layer filled with the rectangular BoN providing $n_{up} = 1.2$ and terminated by a perfectly matched layer (PML). The dimensions w_2 and r_2 of the ridge feed reported in Table I provide an edge-illumination taper of -10 dB at $\phi = \pm 67°$ at the periphery of the lens. The structure has been simulated using a commercial full-wave solver [38]. Fig. 3(c) shows the real part of the vertical component of the electric field in both the lower (left) and the upper PPW (right) at the central frequency of 19.25 GHz. A planar wavefront is clearly formed in the upper PPW, as expected. The far-field performance of the lens in the H-plane is predicted based on the field amplitude and phase distribution across the PML bounded aperture, located in the

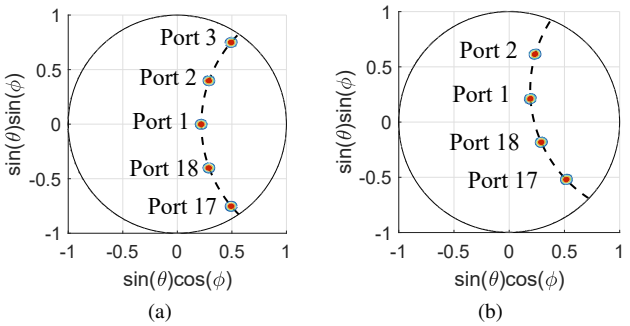

Fig. 4. Scanning contour and principal beam locations for the radiated field at $f = 19.25$ GHz for feeding angles ϕ_{feed} between $-40°$ and $40°$, applicable to ports 17, 18, 1, 2, and 3 (shown in Fig. 3a), during the rotation of the CTS array at (a) $\phi_{\text{rot}} = 0°$ and (b) $\phi_{\text{rot}} = 12°$.

upper PPW. Fig. 3(d) depicts the normalized directivity pattern in the H-plane at the lower frequency (17.3 GHz), central frequency (19.25 GHz), and upper frequency (21.2 GHz) of the band. The lens produces a clear main lobe with a -3 dB beamwidth narrower than $10°$ and SLLs consistently lower than -14 dB across the desired frequency range (from 17.3 to 21.2 GHz). This broadband capability primarily stems from the appropriate choice of the unit-cell providing the graded index.

C. Continuous Transverse Stub Array

The long slots of the CTS are machined on block P3 and are excited by a planar slow-wave wavefront, which is generated by the RLL and propagates in the upper PPW, as described in Sections II-A and II-B. By selecting the excited port, one can change the azimuthal direction of this plane wave. Thus, a linear phase is created along the radiating slots, resulting in a beam direction dependent on the plane wave's angle of incidence. To find the relation between this incidence angle and the beam direction, we introduce a coordinate system $x'Oy'$ relative to the slot orientation, as shown in Fig. 1(c). This reference system rotates along with P3 by an angle ϕ_{rot}. When $\phi_{\text{rot}} = 0°$, the two coordinate systems align, as illustrated in Fig. 1(b), and $\phi' = \phi$. In this scenario, the angle ϕ_s is entirely determined by ϕ_{feed}, which represents the feed's angular orientation relative to the x-axis, as shown in Figs. 1(b) and (c). The x' and y' components of the wavevector $\mathbf{k}$ of the slow Parallel Plate Mode (PPM) in the PPW can be written as

$$k_{x'} = k\cos\phi_s = \frac{2\pi}{\lambda_{\text{guided}}}\cos\phi_s \tag{2}$$

$$k_{y'} = k\sin\phi_s = \frac{2\pi}{\lambda_{\text{guided}}}\sin\phi_s, \tag{3}$$

where λ_{guided} is the guided wavelength in the upper PPW. To determine the scanning properties of the antenna, we utilize the array factor AF of the long slots array [15], calculated as the product $AF = AF_{x'} \times AF_{y'}$ between the array factors along the x' and y' axes, respectively. These factors read as:

$$AF_{x'} = \frac{\sin\left(\frac{Np}{2}(k_0\sin\theta\cos\phi' - k_{x'}\right)}{N\sin\left(\frac{p}{2}(k_0\sin\theta\cos\phi' - k_{x'})\right)} \tag{4}$$

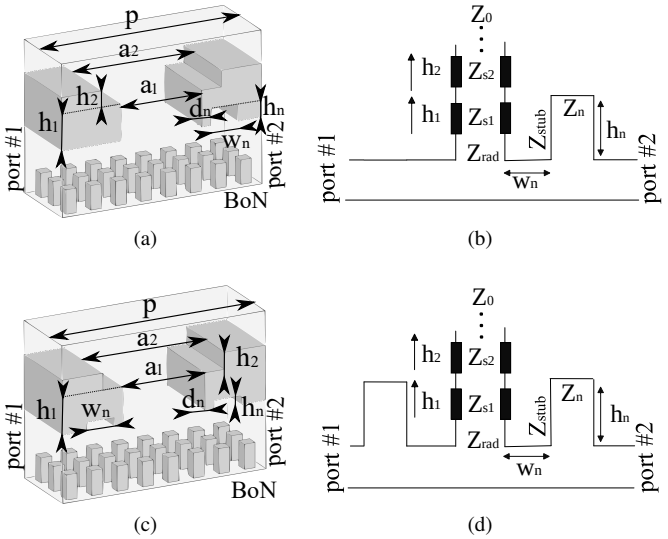

Fig. 5. (a) 3D geometry and (b) equivalent circuit of a CTS unit-cell in a PPW loaded with a BoN with a single reflection-canceling notch. (c) 3D geometry and (d) equivalent circuit of a CTS unit-cell with dual reflection-canceling notches. The the unit-cell design variables are indicated.

$$AF_{y'} = \text{sinc}\left(\frac{L_{\text{slot}}}{2}(k_0\sin\theta\sin\phi' - k_{y'})\right) \tag{5}$$

where ϕ' and θ are the azimuth and elevation angles in the spherical coordinate system in Fig. 1(c), N and p are the number of slots and periodicity along the x'-axis, and k_0 is the free space wavenumber. The quantities $k_{x'}$ and $k_{y'}$ are defined in (2) and (3), respectively. Equation (5) has been derived by considering each slot, with length L_{slot} along the y'-axis, as an array with an infinite number (N_y) of infinitesimally small slots with size p_y, such that $L_{\text{slot}} = N_y p_y$.

The maxima of radiation in the visible space can be found by solving [37]

$$\sin\theta\cos\phi' = \left(\frac{k_{x'}}{k_0} + \frac{2\pi m}{k_0 p}\right), \quad m = 0, \pm1, ..., \pm M. \tag{6}$$

It is clear that the positions of these maxima are determined by the periodicity p and the guided wavenumber k. For broadside pointing and $\phi_{\mathbf{s}} = 0°$, one has $p = -2\pi m/k$, so $m \neq 0$ and we choose $m = -1$ to obtain a single beam. Furthermore, $p < \lambda_0$ to prevent the onset of grating lobes when $m = 0$, which also necessitates a slow wave ($k > k_0$) PPM, as previously discussed. In our case, $k = n_{up}\, k_0$ at the central frequency, which is achieved by implementing an artificial dielectric consisting of a BoN with $h_b = 1.46$ mm, as detailed in Section II-A. The value of $p = 11.2$ mm is chosen to ensure that the main lobes of the array factor produced by the feeds with $\phi_{\text{feed}} = \pm 40°$ remain within the visible spectrum at the lower frequency 17.3 GHz when $\phi_{\text{rot}} = 0°$.

The radiation pattern of the CTS array with radius $R_{\text{CTS}} = 81$ mm can now be computed using p in (2)-(5). The dispersion of the artificial dielectric substrate can also be taken into account in this analysis. Fig. 4(a) illustrates the position of the main beam at $f_1 = 19.25$ GHz when ports 17, 18, 1, 2, and 3 are activated for $\phi_{\text{rot}} = 0$, i.e., the case where the long slots are aligned with the y-axis, as shown in Fig. 1(b).

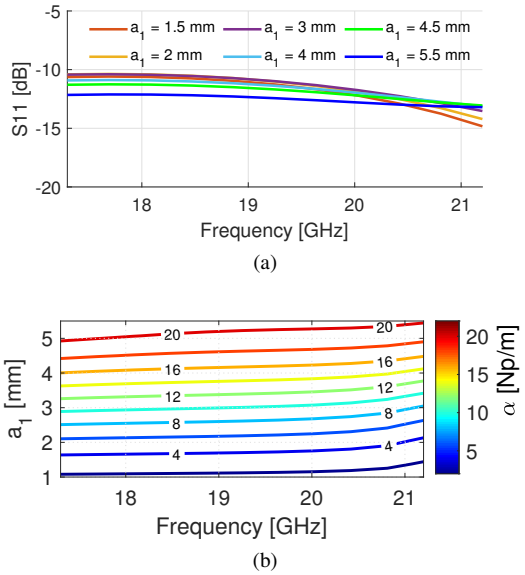

Fig. 6. (a) Magnitude of the input reflection coefficient for the dual-directional unit-cell in Fig. 5(c) as a function of frequency for different values of a_1 and (b) Contour lines showing the attenuation constant α in Np/m as a function of a_1 within the frequency band of interest.

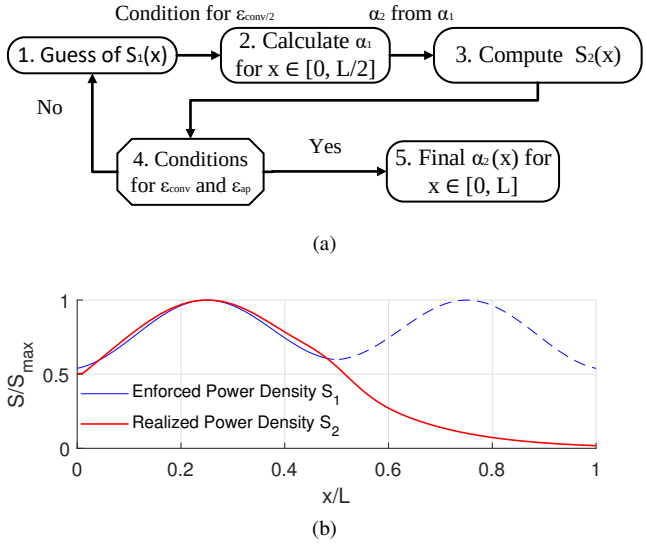

Fig. 7. (a) Flowchart illustrating the algorithm used to derive the total attenuation profile α_2. (b) Comparison between enforced (blue) and realized (red) power density distributions along the direction of propagation.

The dashed line represents the continuous scanning contour obtained from (6). It is shown that the choice of p and n_{up} permits the radiation of 5 beams in this configuration. Next, we consider a mechanical rotation of the upper layer by an angle ϕ_{rot}, as depicted in Fig. 1(c), which leads to a rotation of the scanning contour in the u-v plane ($\phi' = \phi + \phi_{\text{rot}}$). Fig. 4(b) represents the rotated scanning contour and the positions of the main lobes when P3 is rotated by $\phi_{\text{rot}} = 12°$. In this instance, the beam for port 3 (with $\phi_s = \pi - 40° - 12°$) is outside the visible region, reducing the maximum numbers of beams to 4. For every rotation of P3 by ϕ_{rot}, ϕ_s should remain within the $\pi \pm 40°$ range meaning that the excitation of the appropriate feeds is required to potentially cover the entire 2D space.

After determining the scanning capabilities of the array, a slot element that efficiently radiates the slow-wave power is investigated. Fig. 5(a) shows a typical structure for a series-fed CTS unit-cell, consisting of two vertical PPW sections or matching sections, while Fig. 5(b) illustrates the corresponding equivalent circuit model. The first matching section has a height and width of h_1 and a_1, respectively, while the second has a height and width of h_2 and a_2, respectively, to ensure matching to free space. The width of the matching sections (or equivalently the height of the PPWs) must be chosen to ensure uni-modal propagation of the transverse electromagnetic (TEM) mode over the operating frequency range [8]. This condition yields $a_2 < a_{\max} = \frac{c}{2f_{up}}$, where f_{up} is the higher frequency. For $f_{up} = 21.2$ GHz, this results in $a_2 < 7.1$ mm and, in our case, we select $a_2 = 6.7$ mm.

The power radiated by each unit-cell can be controlled by adjusting a_1. Additionally, a single reflection-canceling notch at a distance d_n from the slot is employed to mitigate reflections originating from the radiating slot, targeting a specific direction of propagation for the exciting wavefront. However, in our case, we must ensure reciprocal response when feeding from both port 1 and port 2 in Fig. 5, so a symmetry plane is enforced at the center of the vertical PPW opening. By introducing a second notch, shown in Fig. 5(c) and (d), one can achieve wideband matching of the unit-cell for different values of a_1 in both directions of propagation. Fig. 6(a) shows the magnitude of the input reflection coefficient within the operating frequency band for the optimized dimensions of the reflection-canceling notches ($d_n = 0.5$ mm, $w_n = 1$ mm, and $h_n = 0.6$ mm), and heights of the matching sections ($h_1 = 2.2$ mm and $h_2 = 1.5$ mm). The S_{11} is below -10 dB, which attests to the adequate functioning of this new CTS unit cell.

The attenuation constant for each unit-cell is estimated from its ABCD matrix, which is obtained in turn from the scattering parameters. The complex propagation constant $\gamma = jk = j\beta + \alpha$ is determined by $\cosh(\gamma p) = \frac{A+D}{2}$, a function of the parameters A and D in the transmission matrix. Fig. 6(b) presents the leakage factor α calculated for different slot widths a_1 within the frequency band of interest. The values of α exhibit stable performance with respect to frequency and provide an acceptable range of values to tailor the aperture field distribution in the E-plane.

D. Synthesis of the aperture profile by non-uniform leakage factor

The design of unidirectional series-fed CTS arrays [15], [39] typically aims to achieve a uniform aperture distribution to maximize the aperture efficiency. However, our structure must accommodate excitation from opposite directions, which necessitates a symmetric profile of α. Therefore, enforcing a uniform power distribution, as in [40], is not feasible. To circumvent this issue, the iterative process schematically shown in Fig. 7(a), is followed to find the attenuation profile $\alpha(x)$ that provides a power distribution optimizing the aperture efficiency.

First, let us derive the relationship between the power density distribution and the local attenuation constant. The

TABLE II
GAP a_1 AND ATTENUATION OF CTS ELEMENTS

Stub	# 1	# 2	# 3	# 4	# 5	# 6	# 7
a_1 (mm)	1.37	2.1	2.7	3.26	3.81	4.39	5
α_i (Np/m)	2.8	5.6	8.5	11.3	14.2	17	19.62
Stub	# 8	# 9	# 10	# 11	# 12	# 13	
a_1 (mm)	4.39	3.81	3.26	2.7	2.1	1.37	
α_i (Np/m)	17	14.2	11.3	8.5	5.6	2.8	

power distribution p_{sw} for the slow wave (SW) propagating along the x direction in the PPW underneath the array can be written as [41]:

$$p_{\text{sw}}(x) = p_{\text{sw}}(0)e^{-2\int_0^x \alpha(x')dx'} \tag{7}$$

where $p_{\text{sw}}(0)$ is the power at the input point, and x' is the integration variable. The previous expression can also be written as

$$-\frac{d}{dx}p_{\text{sw}}(x) = -2\alpha(x)p_{\text{sw}}(x) \tag{8}$$

After some derivations, detailed in the Appendix, the profile $\alpha(x)$ providing a desired radiated power density $S_1(x)$ for half of the antenna reads as

$$\alpha_1(x) = \frac{S_1(x)/2}{\frac{p_{\text{sw}}(0)}{p_{\text{sw}}(0)-p_{\text{sw}}(L/2)}\int_0^{L/2} S_1(x')dx' - \int_0^x S_1(x')dx'} \tag{9}$$

The adopted algorithm relies on non-linear optimization [42] and looks for a local minimum. In step 1, we consider a general power density distribution

$$S_1(x) = a_1 \sin\left(\frac{b_1 x}{L} + c_1\right) + a_2 \sin\left(\frac{b_2 x}{L} + c_2\right), \; x \in [0, L/2] \tag{10}$$

After initializing (10) with $a_1 = 14.75$, $b_1 = 0.47$, $c_1 = 1.558$, $a_2 = 1.55$, $b_2 = 9.6$ and $c_2 = -0.14$, one can use (9) to obtain $\alpha_1(x)$ for $x \in [0, L/2]$ in step 2. Then, symmetry is enforced to obtain the attenuation constant for the entire antenna length α_2 by mirroring $\alpha_1(x)$ with respect to the midpoint of the antenna:

$$\alpha_2(x) = \begin{cases} \alpha_1(x) & 0 \le x \le L/2 \\ \alpha_1(-x+L) & L/2 \le x \le L \end{cases} \tag{11}$$

The radiated power per unit length, which can also be seen as the lost portion of the SW power, is related to the final leaky-wave (LW) power density S_2 as follows:

$$p_{\text{lw}}(x) = p_{\text{sw}}(0) - p_{\text{sw}}(x) = \int_0^x S_2(x')dx' \tag{12}$$

In step 3, by differentiating (12) and using (8), the resulting $S_2(x)$ can be expressed in terms of $\alpha_2(x)$ as:

$$S_2(x) = 2\alpha_2(x)p_{\text{sw}}(x) = 2\alpha_2(x)p_{\text{sw}}(0)e^{-2\int_0^x \alpha_2(x')dx'} \tag{13}$$

Finally, we define the conversion efficiency up to the halfway point of the antenna length as $\epsilon_{\text{conv/2}} = \frac{p_{\text{sw}}(0)-p_{\text{sw}}(L/2)}{p_{\text{sw}}(0)}$, while the total conversion efficiency is defined as $\epsilon_{\text{conv}} = \frac{p_{\text{sw}}(0)-p_{\text{sw}}(L)}{p_{\text{sw}}(0)}$. The optimization ends in step 4 when a predefined goal for ϵ_{conv} (obtained from $\epsilon_{\text{conv/2}}$) and the aperture efficiency ϵ_{ap} are both reached. Otherwise, the parameters a_1, b_1, c_1, a_2, b_2 and c_2 are modified and a different profile of $S_1(x)$ is evaluated.

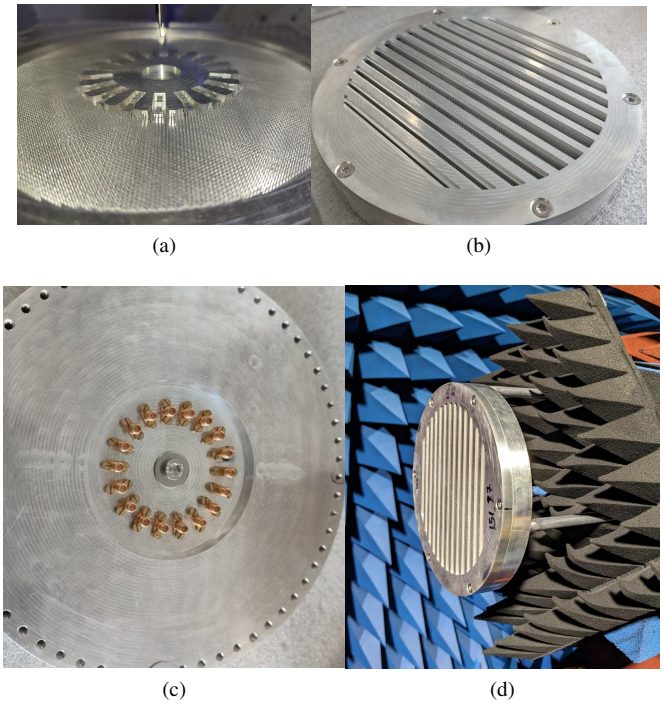

(a) (b) (c) (d)

Fig. 8. (a) CNC milling process shaping the bottom component, which includes the hexagonal unit-cell lattice forming the RLL and the feed network. (b) Completed assembly of the fabricated antenna. (c) Coaxial connectors used to excite the multi-port system. (d) Far-field measurement setup.

Fig. 7(b) shows the power density distributions $S_1(x)$ (red line) and $S_2(x)$ (blue line), based on an initial target efficiency of $\epsilon_{\text{conv/2}} = 0.75$. The efficiencies resulting from the optimization process are $\epsilon_{\text{conv}} = 0.96$ and $\epsilon_{\text{ap}} = 0.83$, which are consistent with the results obtained from other symmetric tapering profile solutions, such as those in [43], and attests to the effectiveness of our optimization strategy. The values of the optimised parameters of (10) are $a_1 = 11.2$, $b_1 = 0.72$, $c_1 = 1.172$, $a_2 = 2.92$, $b_2 = 12$ and $c_2 = -1.37$. The final $S_2(x)$ for the entire antenna length follows the enforced power distribution $S_1(x)$ until the halfway point $L/2$, but the second half of $S_2(x)$ is significantly lower due to the symmetric nature of the attenuation constant. Next, the attenuation profile α_2 is obtained by adapting (9) for the entire antenna length. This profile is then discretized into the number N of long slots along the x-axis, enabling the mapping of α_2 to the appropriate values of the parameter a_1 using the information in Fig. 6(b). Table II displays the slot widths and their corresponding attenuation constant values at the center frequency $f = 19.25$ GHz. These dimensions complete the geometrical definition of the antenna.

III. EXPERIMENTAL RESULTS

The three blocks composing the proposed multi-beam antenna, as defined in Section II and Fig. 1(a), have been fabricated in aluminum ($\sigma = 3.8 \times 10^7$ S/m) using computer numerical control (CNC) milling. Fig. 8(a) shows block P1 during the milling process and the assembled antenna is shown in Fig. 8(b). A central screw from the backside of part P1 (visible in Fig. 8(c)) secures it together with part P2, while 6

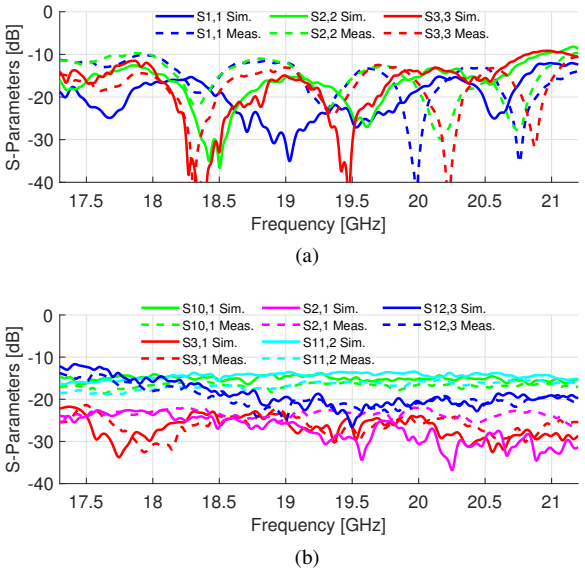

Fig. 9. S-parameters comparison of the antenna system between measured (dashed lines) and simulated values (solid lines) for 0^o rotation of the upper layer. (a) Reflection coefficient of ports 1,2 and 3 and (b) Mutual coupling for ports 1, 2, 3 and 10, 11, 12.

screws spaced at $60°$ intervals around the perimeter join parts P1 and P3. Although only 6 screws are necessary for these parts' mechanical contact, part P1 features 60 screw holes at $6°$ intervals to mimic mechanical rotation by enabling multiple angles ϕ_{rot} between the upper and lower layers.

Fig. 8(c) also shows the 18 coaxial connectors on the backside of part P1; they lie on the inner focal circle and serve to excite the antenna at $20°$ intervals. The complete structure measures $H = 22.7\,\text{mm}$ in thickness ($1.45\lambda_0$ at 19.25 GHz), including the additional $5\,\text{mm}$ for the measurement support. The reduced anisotropy of the hexagonal lattice and the strategic placement of ports yield a symmetric lens and feed system response at $20°$ increments. Hence, we can focus on two upper layer rotation configurations relative to the rest of the system, at $\phi_{\text{rot}} = 0°$ and $12°$. All simulation results in this section have been obtained using CST Microwave Studio [38].

A. S-parameters

The S-Parameters were measured for a $\phi_{\text{rot}} = 0^o$ rotation of the upper part. First, Fig. 9(a) displays the measured (dashed lines) and simulated (solid lines) input reflection coefficients for ports 1, 2 and 3, which fully characterize the antenna due to the symmetry of the structure at $20°$ intervals. The antenna is well matched, displaying a reflection coefficient below -10 dB for the objective frequency band. In turn, Fig. 9(b) presents selected mutual coupling curves for ports 1, 2, 3, 10, 11 and 12. Ports 10, 11 and 12 are diametrically opposed to ports 1, 2 and 3 respectively and have ϕ_{feed} larger by $180°$. In leaky-wave antennas, the non-radiated power is usually absorbed by a load. However, in our case, where we aim to excite the CTS array indistinctly from opposite directions by using two reciprocal ports (e.g. 1 and 10), this solution cannot be used. Here, owing to the RLL design, any non-radiated power is redirected to the opposed port, thus ensuring that energy remains within the bottom PPW and

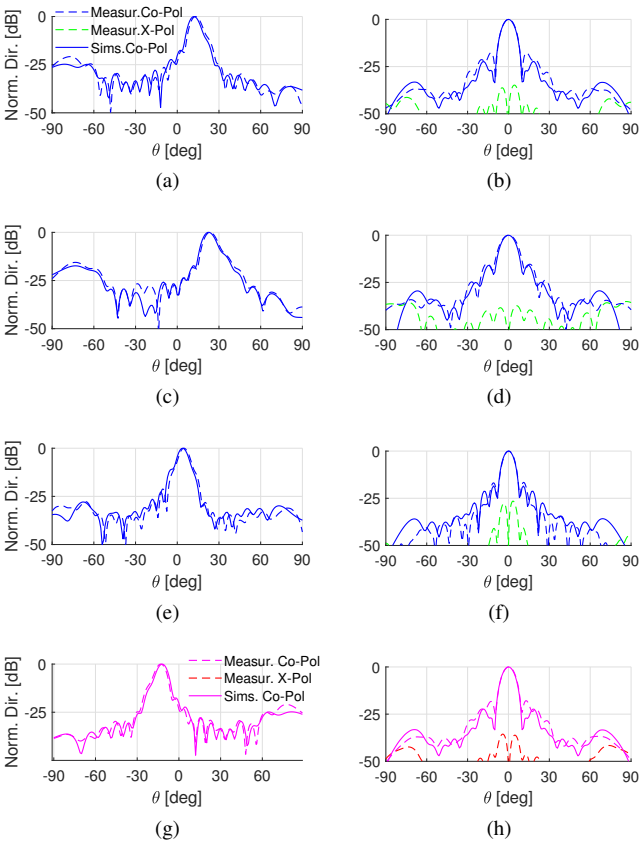

Fig. 10. Comparison between the simulated (co-pol: solid blue line) and measured (co-pol: dashed blue line, cross-pol: dashed green line) normalized directivity in dB when port 1 is excited for the E-plane and H-plane, respectively, at (a)-(b) $f = 19.25$ GHz, (c)-(d) $f = 17.3$ GHz, and at (e)-(f) $f = 21.2$ GHz. Comparison between the simulated (co-pol: solid magenta line) and measured (co-pol: dashed magenta line, cross-pol: dashed red line) normalized directivity in dB when port 10 is excited for (g) the E-plane and (h) H-plane at $f = 19.25$ GHz.

preventing unwanted destructive interference. As mentioned in subsection II-D the system has been designed to radiate more than 90% of the power while maximizing the aperture efficiency, so the power received by reciprocal ports should be below 10%. Fig. 9(b) shows the coupling between the pairs of reciprocal ports 1-10, 2-11 and 3-12 with green, cyan and blue lines respectively. We see indeed that the remaining power gathered by the diametrically opposed ports is attenuated by around -12 to $-16\,\text{dB}$, which represents around 2.5 to 6% of the accepted power. The rest of the (non-reciprocal) ports display a good isolation of around $-25\,\text{dB}$ as showcased by the red and magenta lines in Fig. 9(b).

B. Radiation Patterns

This section first presents the radiation performance of the antenna when port 1, which is aligned with the x-axis at $\phi_{\text{feed}} = 0$, is excited. Figs. 10(a) and (b) display the E- and H-plane normalized directivity patterns, respectively, at the center frequency. Both simulated (solid blue line) and measured results (dashed blue line) are presented. The resulting pencil beam is directed at an azimuth angle of $\phi = 0°$ and elevation angle $\theta = 13°$. Figs. 10(c) and (d) depict the normalized radiation patterns in the E- and H-plane,

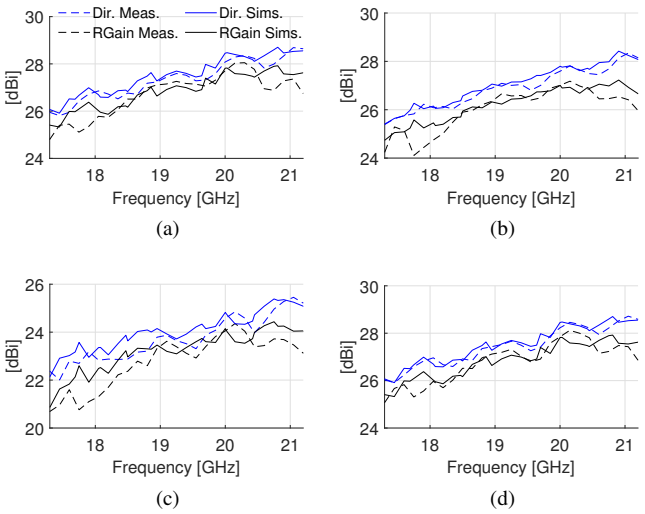

Fig. 11. Comparison of simulated (solid) and measured (dashed) directivity (blue) and realized gain (black) across the frequency band of interest for ports (a) 1, (b) 2, (c) 3, and (d) 10.

respectively, at 17.3 GHz, the lowest frequency of the band. In turn, Figs. 10(e) and (f) showcase the principal cut planes at the upper frequency of 21.2 GHz. All the measured values present an excellent agreement with the simulated ones. The beamwidth and side lobe levels of the H-plane patterns rely on the beamforming capabilites of the RLL. One can see that the beamwidth decreases for increasing frequency, while the SLLs remain below -15 dB within the operating frequency band. On the other hand, the E-plane patterns depend on the CTS leaky wave radiation, with the pointing angle predicted as in subsection II-C. For the slow-wave wavefront parallel to the long slots, as when port 1 is excited, only the elevation angle changes with frequency from $\theta = 4°$ at 21.2 GHz to $\theta = 23°$ at 17.3 GHz. Next, Figs. 10(g) and (h) display the E- and H-plane normalized directivity patterns at the central frequency when port 10, diametrically opposite to port 1, is activated. As expected, the E-plane pattern is the mirrored version of that shown in Fig. 10(a), with a pointing angle of $\theta = -13°$.

Finally, Figs. 11(a), (b), (c) and (d) present the simulated (solid lines) and measured (dashed lines) directivity (blue) and realized gain (black) versus frequency responses for ports 1, 2, 3 and 10, respectively. The agreement between the experimental and predicted results is very good also in this case. The overall aperture efficiency is calculated to be between 43.5-58%, and the radiation efficiency is consistently above 90% across the entire frequency range of interest for port 1. The measured directivity ranges from 25.7 dBi to 28.7 dBi.

C. Scanning Performance

First, the antenna scanning capabilities through port switching are showcased when $\phi_{\text{rot}} = 0°$. Each port is associated with a different ϕ_{feed}, which results in different discrete beam directions in azimuth and elevation along the contour defined by (6). Figs. 12(a)-(c) show the contour plots for the normalized directivity in the $u-v$ plane for ports 1, 2 and 3 at the central frequency, corresponding to ϕ_{feed} angles of $0°, 20°, 40°$. We observe that the main lobe directions follow

TABLE III
MEASURED BEAM LOCATION AT 19.25 GHZ

Port	ϕ_{rot}	Meas. ϕ (Sim. ϕ)	Meas. θ (Sim. θ)
1	0°	1.2°(0°)	13°(12°)
2	0°	53°(54°)	30.5°(30°)
3	0°	55.3°(57°)	64.9°(63°)
10	0°	−1.3°(0°)	−13°(−12°)
11	0°	51.2°(54°)	−31.2°(−30°)
12	0°	54.4°(57°)	−65.5°(−63°)
1	12°	53.7°(59°)	22.8°(20°)
18	12°	−20.8°(−26°)	18°(16°)
17	12°	−42.3°(−45°)	42°(40°)
2	12°	66.5°(69°)	48.8°(47°)

the predicted scanning contours, represented by the dashed white lines. Due to the symmetry of the structure, the beams for ports 17 and 18 are those of ports 3 and 2 mirrored with respect to the u axis. Additionally, ports 8-12 provide beams that are those of ports 3, 2, 1, 18 and 17 mirrored with respect to the v axis, which results in a total number of 10 beams in the visible region. Table III presents the discrete beam positions. In Fig. 11 we can see that the directivity and realized gain of these beams also correspond to the simulations. Due to the beam for port 3 being directed at 65° in elevation, the effective aperture, and therefore the directivity, are lower. The description of the $\phi_{\text{rot}} = 0°$ configuration is completed by examining the effect of frequency scanning when different ports are excited. Table IV illustrates how the direction of the radiated beam changes with frequency in both elevation and azimuth for ports 1, 2, and 3. The values $\Delta\phi$ and $\Delta\theta$ indicate the changes in pointing direction in azimuth and elevation, respectively, relative to the central frequency (19.25 GHz) for each port. For completeness, the normalized directivity in the u-v plane is included in Fig. S1 of the Supplementary Material for ports 1, 2 and 3, at both the lower ($f = 17.3$ GHz) and higher frequencies ($f = 21.2$ GHz).

TABLE IV
MEASURED FREQUENCY SCANNING FOR PORTS 1, 2 AND 3

Port	17.3 GHz	19.25 GHz	21.2 GHz
1	ϕ : 0° $\Delta\phi$: −1.2° θ : 23.6° $\Delta\theta$: 10.6°	ϕ : 1.2° $\Delta\phi$: 0° θ : 13° $\Delta\theta$: 0°	ϕ : 3.3° $\Delta\phi$: 2.1° θ : 4.9° $\Delta\theta$: −8.1°
2	ϕ : 39.8° $\Delta\phi$: −13.2° θ : 38.7° $\Delta\theta$: 8.2°	ϕ : 53° $\Delta\phi$: 0° θ : 30.5° $\Delta\theta$: 0°	ϕ : 68.1° $\Delta\phi$: 15.1° θ : 26.2° $\Delta\theta$: −4.3°
3	ϕ : 48.2° $\Delta\phi$: −7.1° θ : 73.7° $\Delta\theta$: 8.8°	ϕ : 55.3° $\Delta\phi$: 0° θ : 64.9° $\Delta\theta$: 0°	ϕ : 63.1° $\Delta\phi$: 7.8° θ : 57.2° $\Delta\theta$: −7.7°

Second, we explore continuous scanning by rotating the CTS on the upper layer. To achieve this, we apply a rotation of the top layer equal to $\phi_{\text{rot}} = 12°$, resulting in a rotation of the scanning contour in the $u-v$ plane as explained in Section II-C. Figs. 12 (d)-(e) depict the normalized directivity in the $u-v$ plane for ports 1, 18 and 17, respectively, at $f = 19.25$ GHz. In this configuration, port 3 does not radiate as the angle ϕ_s between the propagating wavefront and the CTS orientation is too large. This results in only 8 beams in the visible region, from ports 1, 2, 18 17, and their diametrically

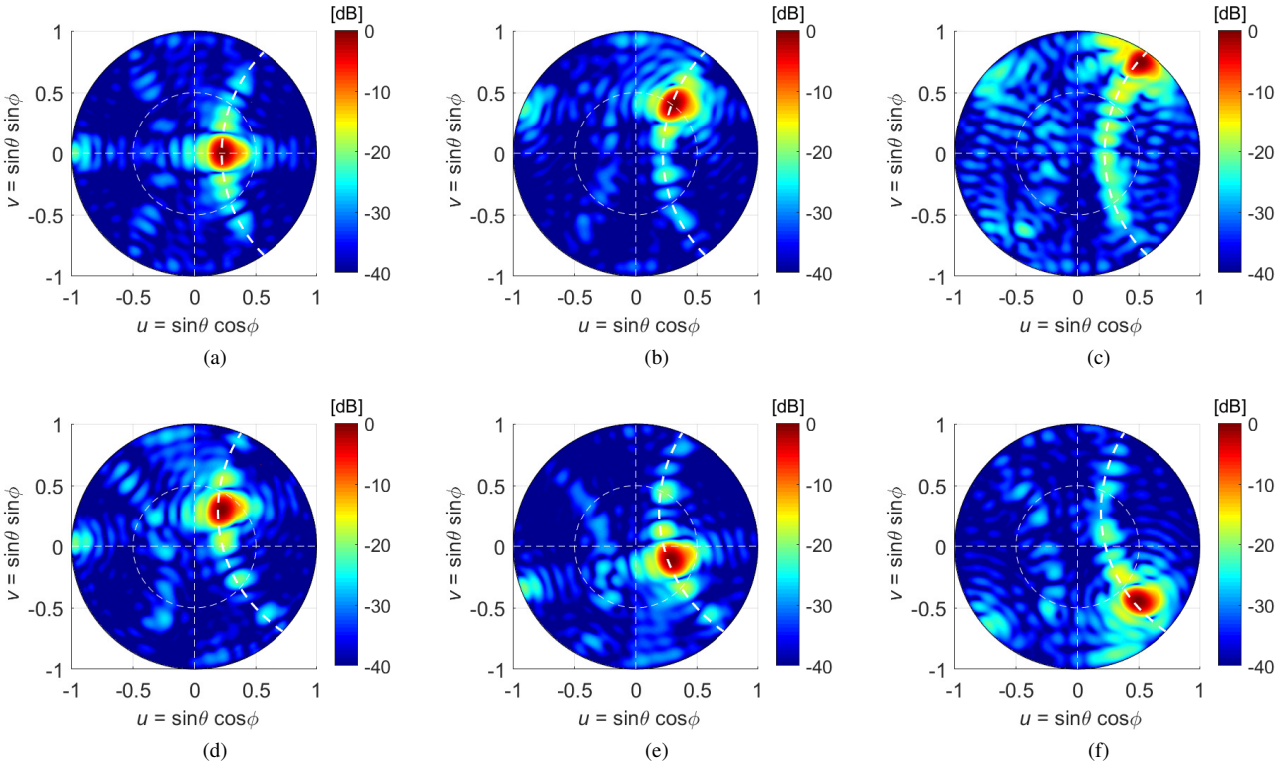

Fig. 12. Measured beamscanning performance in $u-v$ plane at the central frequency $f = 19.25$ GHz for 0^o rotation of the upper layer when (a) port 1, (b) port 2 and (c) port 3 are excited. For a 12^o rotation of the upper layer when (d) port 1, (e) port 18 and (f) port 17 are excited.

opposed counterparts. It is demonstrated that the measured beam positions fall again on the predicted scanning contour, represented by the white dashed line. The continuous rotation of the scanning contour is dependent on ϕ_{rot}, whereas scanning along the contour is determined by the discrete values of the feeds ϕ_{feed}. The beam in this case scans along the contour in discrete steps the azimuth from $-42.2°$ to $66.5°$ and the elevation from $18°$ to $48.8°$, also presented in Table III.

Table V presents the key performance metrics for recent CTS arrays defining the state-of-the-art and reported in the open literature, as well as for our design. Our solution enables, for the first time, the excitation of the CTS from opposite directions. This results in a significant increase in the number of simultaneous beams. Compared to the multibeam solution in [16] and [17], which provide 5 and 4 simultaneous beams respectively, we double the number of beams, achieving up to 10. In addition, we show that it is possible to concurrently utilize multibeam operation alongside mechanical scanning to enhance the coverage provided by other CTS arrays that rely solely on mechanical rotation for scanning [15], [20].

IV. Conclusion and Discussion

This paper introduces, for the first time, the use of a reflecting Luneburg lens as a beamformer for multibeam operation of a continuous transverse stub (CTS) array. It has been demonstrated that this double-layer solution doubles the number of simultaneous beams compared to other examples in the open literature. To achieve this, the reflecting Luneburg lens in the bottom PPW features a circular array of 18 feeds in its inner focal region. The RLL's GRIN medium is implemented by a BoN with a hexagonal lattice for improved isotropy, thereby better leveraging the lens's capability of generating planar wavefronts with arbitrary directions in the top layer. To effectively radiate the power impinging from multiple directions on the series dual-fed CTS array, a novel unit cell has been also proposed to offer good matching when excited from opposite directions. Moreover, an optimization framework has been presented to maximize the radiation and aperture efficiencies of the proposed antenna system.

The experimental results confirm the predictions, showing good matching and isolation between ports. The measured directivity for the main port ranges from 25.7 to 28.7 dBi between 17.3 GHz and 21.2 GHz, corresponding to a 43.5-58% aperture efficiency. Additionally, this all-metal antenna demonstrates excellent radiation efficiency, exceeding 90% across the band, and constitutes a robust solution well-suited for harsh environments. Alongside the inherent frequency scanning of series-fed CTS arrays, the measurement campaign has also demonstrated the antenna's scanning capabilities. Initially, we demonstrate that our system can generate up to 10 simultaneous beams through port switching, surpassing current multibeam limits documented in the literature. Subsequently, through mechanical rotation of the CTS block, each of these beams can be continuously directed in different directions, as shown here in the case of a $12°$ rotation. By combining port switching with mechanical scanning, this antenna significantly expands the current scanning limitations of CTS systems, providing full 2D scanning coverage.

TABLE V
SUMMARY OF THE STATE-OF-THE-ART ON VICTS ARRAYS

Ref.	Peak Gain (dBi)	BW (GHz)	Scan Range (°)	Dimensions	Scanning Method	Rad. Eff.(%)	Silm. Beams
[18]	18.1	8.5 – 14.1	−16.8 to 55.2	$11.7\lambda_0 \times 1.28\lambda_0 \times 0.24\lambda_0$ 292 mm × 32 mm × 6 mm	Frequency Scan	NA	1
[16]	20.9	33 – 37	±38, ±69	$4.1\lambda_0 \times 4.8\lambda_0 \times 0.24\lambda_0$ 35.1 mm × 41.1 mm × 2 mm	Port Switch	87.1	5
[17]	31	23 – 25	±15	$23\lambda_0 \times 23\lambda_0 \times 1.68\lambda_0$ 288 mm × 288 mm × 21 mm	Port Switch	79.9	4
[15]	29.3	59 – 63	±60	$11.7\lambda_0 \times 11.7\lambda_0 \times 1.92\lambda_0$ 57 mm × 57 mm × 9.35 mm	Mechanical Rot.	82.2	1
[20]	24.2	19.2 – 20.4	±38	$7.3\lambda_0 \times 6.5\lambda_0 \times 0.65\lambda_0$ 111 mm × 99.7 mm × 10 mm	Mechanical Rot.	90	1
[20]	28.5	28.4 – 30	±60	$10.8\lambda_0 \times 9.7\lambda_0 \times 0.97\lambda_0$ 111 mm × 99.7 mm × 10 mm	Mechanical Rot.	90	1
This work	28.7	17.3 – 21.2	±63	$12.8\lambda_0 \times 12.8\lambda_0 \times 1.45\lambda_0$ 200 mm × 200 mm × 22.7 mm	Port Switch & Mech. Rot.	90	8-10

APPENDIX A

To obtain the α profile providing a desired radiated power density $S_1(x)$ for half of the antenna, we first differentiate (7):

$$\frac{d}{dx}p_{\text{lw}}(x) = -\frac{d}{dx}p_{\text{sw}}(x) = -2\alpha(x)p_{\text{sw}}(x) = KS(x) \quad (14)$$

where K is a proportionality constant.

Next, we integrate (14) to obtain:

$$\begin{aligned} \int_0^x dp_{sw}(x') &= -K\int_0^x S(x')d\,x' \\ \Rightarrow p_{sw}(0) - p_{sw}(x) &= K\int_0^x S(x')dx' \end{aligned} \quad (15)$$

$$\begin{aligned} \int_0^{L/2} dp_{sw}(x') &= -K\int_0^{L/2} S(x')d\,x' \\ \Rightarrow p_{sw}(0) - p_{sw}(L/2) &= K\int_0^{L/2} S(x')dx' \end{aligned} \quad (16)$$

and solve for K in (16):

$$K = \frac{p_{\text{sw}}(0) - p_{\text{sw}}(L/2)}{\int_0^{L/2} S(x)dx} \quad (17)$$

By inserting (15), (17), and (7) into (8), we obtain α as in (9).

ACKNOWLEDGMENT

The authors are grateful to Dr. L. Le Coq and Frédéric Boutet (M^2ARS platform, IETR, Univeristé de Rennes) for conducting the radiation pattern measurements.

REFERENCES

[1] I. F. Akyildiz, A. Kak, and S. Nie, "6G and Beyond: The Future of Wireless Communications Systems," *IEEE Access*, vol. 8, p. 36, 2020.
[2] R. A. Pearson, J. Vazquez, M. W. Shelley, A. Payne, V. Stoiljkovic, and M. Steel, "Next generation mobile SATCOM terminal antennas for a transformed world," in *Proc. 5th Eur. Conf. Antennas propag. (EuCAP)*, Apr. 2011, pp. 2341–2345.
[3] G. Toso, C. Mangenot, and P. Angeletti, "Recent advances on space multibeam antennas based on a single aperture," in *Proc. 7th eur. Conf. Antennas propag. (EuCAP)*, 2013, pp. 454–458.
[4] N. E. Lindenblad, "Multiple slot antenna," US Patent US2 628 311A, Feb., 1953.
[5] W. W. Milroy, "The continuous transverse stub (CTS) array: Basic theory," *Proc. Antennas Appl. Symp.*, vol. 2, pp. 253–283, Nov. 1991.
[6] ——, "Continuous transverse stub element devices and methods of making same," US Patent US5 266 961A, Nov., 1993.
[7] ——, "Antenna array configurations employing continuous transverse stub elements," US Patent US5 349 363A, Sep., 1994.
[8] M. Ettorre, F. F. Manzillo, M. Casaletti, R. Sauleau, L. L. Coq, and N. Capet, "Continuous transverse stub array for Ka-Band applications," *IEEE Trans. Antennas Propag.*, vol. 63, no. 11, pp. 4792–4800, Nov. 2015.
[9] T. Potelon *et al.*, "A low-profile broadband 32-slot continuous transverse stub array for backhaul applications in E -band," *IEEE Trans. Antennas Propag.*, vol. 65, no. 12, pp. 6307–6316, Dec. 2017.
[10] T. Potelon, M. Ettorre, L. Le Coq, T. Bateman, J. Francey, and R. Sauleau, "Reconfigurable CTS antenna fully integrated in PCB technology for 5G backhaul applications," *IEEE Trans. Antennas Propag.*, vol. 67, no. 6, pp. 3609–3618, Jun. 2019.
[11] W. Wang, Q. Huang, Z. Liu, H. Liu, and X. Shi, "A beam scanning continuous transverse stub array antenna for Ka-band applications," *Microw. Opt. Technol. Lett.*, vol. 61, no. 4, pp. 1097–1103, 2019.
[12] T. Potelon, M. Ettorre, T. Bateman, J. Francey, and R. Sauleau, "Broadband passive two-feed-per-beam pillbox architecture for high beam crossover level," *IEEE Trans. Antennas Propag.*, vol. 68, no. 1, pp. 575–580, Jan. 2020.
[13] M. Śmierzchalski *et al.*, "A novel dual-polarized continuous transverse stub antenna based on corrugated waveguides—part ii: Experimental demonstration," *IEEE Trans. Antennas Propag.*, vol. 69, no. 3, pp. 1313–1323, 2021.
[14] M. Del Mastro *et al.*, "Ultra-low-profile continuous transverse stub array for satcom applications," *IEEE Trans. Antennas Propag.*, vol. 70, no. 6, pp. 4459–4471, 2022.
[15] K. Tekkouk, J. Hirokawa, R. Sauleau, and M. Ando, "Wideband and large coverage continuous beam steering antenna in the 60-GHz band," *IEEE Trans. Antennas Propag.*, vol. 65, no. 9, pp. 4418–4426, Sep. 2017.
[16] S.-C. Sun, Y.-J. Zhao, Y.-Z. Zheng, N.-X. Zhou, and Y.-L. Ban, "A continuous transverse stub array with parabolic reflector for Ka-band multibeam application," *AEU - Int. J. Electron. Commun.*, vol. 170, p. 154818, Oct. 2023.
[17] L. Yan, W. Zou, K. Zheng, G. Yang, and Y. Luo, "A dual-polarized CTS array antenna with four reconfigurable beams for mm-wave wind profile radar," *Electronics*, vol. 13, no. 1, p. 238, Jan. 2024.
[18] X.-X. Yang, L. Di, Y. Yu, and S. Gao, "Low-profile frequency-scanned antenna based on substrate integrated waveguide," *IEEE Trans. Antennas Propag.*, vol. 65, no. 4, pp. 2051–2056, Apr. 2017.
[19] W. W. Milroy, "Variable Inclination stub array," *US Patent 6 919 854*, Jul. 2005.
[20] R. S. Hao, Y. J. Cheng, and Y. F. Wu, "Shared-Aperture Variable Inclination Continuous Transverse Stub Antenna Working at *K* - and *Ka* -Bands for Mobile Satellite Communication," *IEEE Trans. Antennas Propag.*, vol. 68, no. 9, pp. 6656–6666, Sep. 2020.
[21] W. Rotman, "Wide-angle scanning with microwave double-layer pillboxes," *IRE Trans. Antennas Propag.*, vol. 6, no. 1, pp. 96–105, Jan. 1958.
[22] M. Ettorre, R. Sauleau, and L. Le Coq, "Multi-beam multi-layer leaky-wave SIW pillbox antenna for millimeter-wave applications," *IEEE Trans. Antennas Propag.*, vol. 59, no. 4, pp. 1093–1100, Apr. 2011.

[23] Y. J. Park, A. Herschlein, and W. Wiesbeck, "A photonic bandgap (PBG) structure for guiding and suppressing surface waves in millimeter-wave antennas," *IEEE Trans. Microw. Theory Tech.*, vol. 49, no. 10, pp. 1854–1859, Oct. 2001.
[24] C. Pfeiffer and A. Grbic, "A printed, broadband Luneburg lens antenna," *IEEE Trans. Antennas Propag.*, vol. 58, no. 9, pp. 3055–3059, 2010.
[25] M. Bosiljevac, M. Casaletti, F. Caminita, Z. Sipus, and S. Maci, "Non-uniform metasurface luneburg lens antenna design," *IEEE Trans. Antennas Propag.*, vol. 60, no. 9, pp. 4065–4073, 2012.
[26] Y. B. Li, R. Y. Wu, W. Wu, C. B. Shi, Q. Cheng, and T. J. Cui, "Dual-physics manipulation of electromagnetic waves by system-level design of metasurfaces to reach extreme control of radiation beams," *Adv. Mater. Technol.*, vol. 2, no. 1, p. 1600196, 2017.
[27] A. B. Numan, J.-F. Frigon, and J.-J. Laurin, "Printed W-band multibeam antenna with luneburg lens-based beamforming network," *IEEE Trans. Antennas Propag.*, vol. 66, no. 10, pp. 5614–5619, 2018.
[28] D. Pérez-Quintana *et al.*, "Fully metallic Luneburg metalens antenna in gap waveguide technology at V-band," *IEEE Trans. Antennas Propag.*, vol. 71, no. 4, pp. 2930–2937, Apr. 2023.
[29] A. Mahmoud, J. Ruiz-García, O. de Sagazan, M. Ettorre, R. Sauleau, and D. González-Ovejero, "Low-cost and low-profile sub-terahertz luneburg lens beamformer on polymer," *IEEE Antennas Wireless Propag. Lett.*, vol. 22, no. 6, pp. 1411–1415, 2023.
[30] J. Ruiz-García, E. Martini, C. D. Giovampaola, D. González-Ovejero, and S. Maci, "Reflecting Luneburg lenses," *IEEE Trans. Antennas Propag.*, vol. 69, no. 7, pp. 3924–3935, Jul. 2021.
[31] Q. Chen, S. A. R. Horsley, N. J. G. Fonseca, T. Tyc, and O. Quevedo–Teruel, "Double-layer geodesic and gradient-index lenses," *Nat Commun*, vol. 13, no. 1, p. 2354, Dec. 2022.
[32] C. Bilitos, X. Morvan, E. Martini, R. Sauleau, S. Maci, and D. González-Ovejero, "Broadband reflecting Luneburg lenses based on bed-of-nails metasurfaces," *IEEE Trans. Antennas Propag.*, vol. 72, no. 2, pp. 1923–1928, Feb. 2024.
[33] K. C. Chen, J. W. Yang, Y.-C. Yang, C. F. Khin, and M. N. M. Kehn, "Plasmonic Luneburg lens antenna synthesized by metasurfaces with hexagonal lattices," *Opt. Express*, vol. 25, no. 22, pp. 27 405–27 414, Oct. 2017.
[34] J. D. de Pineda, R. C. Mitchell-Thomas, A. P. Hibbins, and J. R. Sambles, "A broadband metasurface Luneburg lens for microwave surface waves," *Appl. Phys. Lett.*, vol. 111, no. 21, p. 211603, 11 2017.
[35] S. Yang, O. Zetterstrom, F. Mesa, and O. Quevedo-Teruel, "Dispersion Analysis of Metasurfaces With Hexagonal Lattices With Higher Symmetries," *IEEE J. Microw.*, vol. 3, no. 4, pp. 1154–1165, Oct. 2023.
[36] ANSYS Inc., "HFSS, version 2020 R1," Pittsburgh, PA, 2020.
[37] A. Bhattacharyya, "Theory of beam scanning for slot array antenna excited by slow wave," *IEEE Antennas Propag. Mag.*, vol. 57, no. 2, pp. 96–103, Apr. 2015.
[38] CST of America, "CST Microwave Studio," Anaheim, CA, 2020.
[39] R. Thanikonda, D. González-Ovejero, G. Toso, E. Martini, and S. Maci, "High-efficiency low profile full-metal cts array for satcom," in *IEEE Microw. Antennas Propag. Conf. (MAPCON)*, 2023, pp. 1–4.
[40] G. Minatti, E. Martini, and S. Maci, "Efficiency of metasurface antennas," *IEEE Trans. Antennas Propag.*, vol. 65, no. 4, pp. 1532–1541, 2017.
[41] D. R. Jackson and A. A. Oliner, "Leaky-wave antennas," in *Modern Antenna Handbook*, C. A. Balanis, Ed. John Wiley & Sons, Ltd, 2008, ch. 7, pp. 325–367.
[42] J. C. Lagarias, J. A. Reeds, M. H. Wright, and P. E. Wright, "Convergence properties of the nelder-mead simplex method in low dimensions," *SIAM J. Optim.*, vol. 9, pp. 112–147, 1998. [Online]. Available: https://api.semanticscholar.org/CorpusID:9245771
[43] A. Gil-Martinez, M. Poveda-García, D. Cañete-Rebenaque, O. Quevedo-Teruel, and J. L. Gómez-Tornero, "Symmetric tapering of bi-directionally fed leaky-wave antennas for multi-beam synthesis," in *17th Eur. Conf. Antennas Propag. (EuCAP)*, 2023, pp. 1–5.

Christos Bilitos was born in Serres, Greece, in 1994. He received his M.S. degree in telecommunication engineering from Aristotle University of Thessaloniki, Thessaloniki, Greece, in April 2018, and his Ph.D. degree in electronics from the University of Rennes, Rennes, France, in 2024.

From 2018 to 2020, he worked in industry before pursuing his Ph.D. studies at the Institut d'Electronique et des Technologies du numéRique (IETR), Rennes, France, in collaboration with the Agence Innovation Défense (AID), where he is currently a Post-Doctoral Researcher. During his Ph.D. studies, he spent four months as a visiting scholar at the University of Siena in 2021 and 2022.

His research interests include computational electromagnetics, leaky-wave structures, metasurfaces, and quasi-optical beamformers for mm-wave antennas.

Xavier Morvan graduated in mechanical and production engineering from the University Institute of Technology of Brest in 2001. He went on studying in mechanics in the IUP always in Brest until 2003. In 2005, he joined the Institute of Electronics and Telecommunications of Rennes (IETR) to work on special machines in microelectronics. From 2008, he has been involved in the realization of antennas, he is a specialist in high speed machining of mechanical parts for antennas in the 1 GHz to 300 GHz range and in additive manufacturing.

Ronan Sauleau (M'04–SM'06–F'18) got his post-graduate degree and M.Sc. in electrical engineering and radio communications from the Institut National des Sciences Appliquées, Rennes, France, in 1995. He received the Agrégation degree from the Ecole Normale Supérieure de Cachan, France, in 1996, and the Doctoral degree in signal processing and telecommunications and the "Habilitation à Diriger des Recherches" degree, both from the University of Rennes 1, France, in 1999 and 2005, respectively. He was an Assistant Professor and Associate Professor at the University of Rennes 1, between September 2000 and November 2005, and between December 2005 and October 2009, respectively. He has been appointed as a full Professor in the same University since November 2009. His current research fields are numerical modeling, millimeter-wave beam steering antennas, substrate integrated waveguide antennas, lens-based focusing devices, periodic and non-periodic structures (FSS, metasurfaces, polarizers, reflectarrays, and transmitarrays) and biological effects of millimeter waves.

He has been involved in more than 80 research projects at the national and European levels and has co-supervised 29 post-doctoral fellows, 63 PhD students and 50 master students. He has received 25 patents and is the author or coauthor of 300 journal papers and more than 600 publications in international conferences and workshops. He was co-director of the research Department 'Antenna and Microwave Devices' at IETR and deputy director of IETR between 2012 and 2016. He is now director of IETR. Prof. Sauleau received the 2004 ISAP Conference Young Researcher Scientist Fellowship (Japan) and the first Young Researcher Prize in Brittany, France, in 2001 for his research work on gain-enhanced Fabry-Perot antennas. In September 2007, he was elevated to Junior member of the "Institut Universitaire de France". He was awarded the Bronze medal by CNRS in 2008, and the silver medal in 2020. He received the 2021 Antenna EurAAP Award. He was the co-recipient of several international conference awards with some of his students (Int. Sch. of BioEM 2005, BEMS'2006, MRRS'2008, E-MRS'2011, BEMS'2011, IMS'2012, Antem'2012, BioEM'2015, EuCAP'2019, EuCAP'2021, EuMW'2022). He served as a guest editor for the IEEE Antennas Propogat. Special Issue on "Antennas and Propagation at mm and sub mm waves". He served as a national delegate for several EU COST actions. He has served as a national delegate for EurAAP and as a member of the board of Director of EurAAP from 2013 to 2018.

Enrica Martini (S'98-M'02-SM'13) was born in Spilimbergo (PN), Italy, in 1973. She received the Laurea degree (cum laude) in telecommunication engineering from the University of Florence, Italy, in 1998. From 1998 to 1999 she worked at the University of Florence under a one-year research grant from the Alenia Aerospazio Company, Rome, Italy. In 2002, she received the PhD degree in informatics and telecommunications from the University of Florence and the Ph.D. degree in electronics from the University of Nice-Sophia Antipolis, under joint supervision. In 2002, she was appointed Research Associate at the University of Siena, Italy. In 2005, she received the Hans Christian Ørsted Postdoctoral Fellowship from the Technical University of Denmark, Lyngby, Denmark, and she joined the Electromagnetic Systems Section of the Ørsted•DTU Department until 2007. From 2007 to 2017 she was a Postdoctoral Fellow at the University of Siena, Italy. In 2012, she co-founded the start-up Wave Up Srl, Siena, Italy, of which she was the CEO from 2016 to 2018. From 2019 to 2021 she was an assistant professor at the University of Siena, Italy. She is currently an Associate Professor with the Department of Information Engineering and Mathematics, University of Siena, Siena, Italy.

Dr. Martini coordinated tasks of various research projects funded by national and international governmental institutions, as well as by industry. Her research interests include metasurfaces and metamaterial characterization, metasurface-based antennas and microwave devices, electromagnetic scattering, antenna measurements and tropospheric propagation. Dr. Martini was a co-recipient of the 2016 Schelkunoff Transactions Prize Paper Award, of the Best Paper Award in Antenna Design and Applications at the 11th European Conference on Antennas and Propagation in 2017, of the Best Poster Award at the Metamaterials Congress in 2019 and of the Best Paper Award in Electromagnetics at the 15th European Conference on Antennas and Propagation in 2021.

Stefano Maci (M'92–SM'99–F'04) received the Laurea degree (cum laude) from the University of Florence, Florence, Italy, in 1987. Since 1997, he has been a Professor at the University of Siena, Siena, Italy. Currently, he leads a group of 15 researchers at this university. His research activity is reflected in his publication record comprising 200 papers in international journals, 14 book chapters, and about 600 papers in proceedings of international conferences. His interests encompass high-frequency and beam representation methods, computational electromagnetics, large phased arrays, planar antennas, reflector antennas and feeds, metamaterials, and metasurfaces. From 2008 to 2015, he was the Director of the Ph.D. Program in information engineering and mathematics at the University of Siena, coordinating 60 Ph.D. students of all areas per year.

Prof. Maci served as a member of the Technical Advisory Board for 20 international conferences. He has been a member of the Review Board for six international journals. From 2004 to 2007, he was one of the leaders of the Antenna Center of Excellence (ACE, FP6-EU), and from 2007 to 2010, he was an International Coordinator of a 24-Institution Consortium of a Marie Curie Action (FP6). In 2004, he founded the European School of Antennas (ESoA), a post-graduate school that currently offers 34 courses on antennas, propagation, electromagnetic theory, and computational electromagnetics. With 150 teachers from 15 countries, he has been the Director of ESoA since its inception. He was a member of the Administrative Committee (AdCom) of the IEEE Antennas and Propagation Society (AP-S) from 2012 to 2014, an Associate Editor of the IEEE Transactions on Antennas and Propagation, the Chair of the Awards Committee of IEEE AP-S, and a member of the Board of Directors of the European Association on Antennas and Propagation (EurAAP). He was also a member of the Antennas and Propagation Executive Board of the Institution of Engineering and Technology (IET, U.K.). He served as the President for the IEEE Antennas and Propagation Society in 2023. He has been actively involved in various projects, including founding and directing the consortium FORESEEN from 2014 to 2018, which involved 48 European institutions. He served as the Principal Investigator for the Future Emerging Technology Project "Nanoarchitectronics" of the 8th EU Framework Program and the EU Program "Metamask." Since 2010, he has been the Principal Investigator of other 50 projects and university coordinator, 15 of them financed by the European Space Agency. He co-founded two spin-off companies. He has been a Distinguished Lecturer of the IEEE Antennas and Propagation Society (AP-S) and the EuRAAP Distinguished Lecturer in the Ambassador Program. In recognition of his outstanding contributions, he received the EurAAP Award in 2014, the IEEE Schelkunoff Transaction Prize in 2016, the Chen-To Tai Distinguished Educator Award in 2016, and the URSI Dellinger Gold Medal in 2020. In the last decade, he has been invited 50 times as a keynote speaker or a distinguished lecturer at international conferences. He has been the TPC Chair of the 2020 METAMATERIAL Conference and the General Chairperson of the European Conference on Antennas and Propagation (EuCAP) in 2023.

David González-Ovejero (S'01–M'13–SM'17) received the M.Sc. degree in telecommunication engineering from the Universidad Politécnica de Valencia, Valencia, Spain, in 2005, the Ph.D. degree in electrical engineering from the Université catholique de Louvain, Louvain-la-Neuve, Belgium, in 2012, and the Habilitation à Diriger des Recherches degree from the Université de Rennes in 2024. From 2012 to 2014, he was a Research Associate at the University of Siena, Siena, Italy. In 2014, he joined the Jet Propulsion Laboratory, California Institute of Technology, Pasadena, CA, USA, where he was a Marie Curie Post-Doctoral Fellow. Since 2016, he has been a tenured researcher at the French National Center for Scientific Research (CNRS), Institut d'Electronique et des Technologies du numéRique (IETR), Rennes, France. His current research interests include computational electromagnetics, large phased arrays, periodic structures, metasurfaces, and submillimeter-wave antennas.

Dr. González Ovejero was awarded a Marie Curie International Outgoing Fellowship from the European Commission in 2013, the Sergei A. Schelkunoff Transactions Prize Paper Award from the IEEE Antennas and Propagation Society in 2016, the Best Paper Award in Antenna Design and Applications at the 11th European Conference on Antennas and Propagation in 2017, the Best Paper Award in Electromagnetics at the 15th European Conference on Antennas and Propagation in 2021, and the Best Paper Award at the International Workshop on Antenna Technology (iWAT) in 2023. Since 2019, he has served as an Associate Editor of the IEEE TRANSACTIONS ON ANTENNAS AND PROPAGATION and the IEEE TRANSACTIONS ON TERAHERTZ SCIENCE AND TECHNOLOGY.